Mechanochromic Palettes of Cholesteric Liquid Crystal Elastomers for Visual Signaling

Park, Hyewon
Lee, Hye Joo
Ahn, Hyungju
Lee, Young-Joo
Yun, Hee Seong
Choi, Yunseok
Kim, Dae Seok
Yoon, Dong Ki

To be published in: Advanced Optical Materials

DOI to publisher's version: 10.1002/adom.202400266

Mechanochromic Palettes of Cholesteric Liquid Crystal Elastomers for Visual Signaling

Hyewon Park†, Hye Joo Lee†, Hyungju Ahn, Woong Chan Han, Hee Seong Yun, Yun-Seok Choi, Dae Seok Kim*and Dong Ki Yoon**

H. Park, H. S. Yun, Prof. D. K. Yoon
Department of Chemistry, Korea Advanced Institute of Science and Technology (KAIST), Daejeon, 34141, Republic of Korea
E-mail: nandk@kaist.ac.kr

H. J. Lee, W. C. Han, Prof. D. S. Kim
Department of Polymer Engineering, Pukyong National University, Busan, 48513, Republic of Korea
E-mail: daeseok@pknu.ac.kr

Dr. H. Ahn
Pohang Accelerator Laboratory, Pohang 37673, Republic of Korea

Dr. Y.-S. Choi
Center for Integrated Nanotechnologies, Los Alamos National Laboratory, Los Alamos, NM 87545, United States of America
E-mail: yun_choi@lanl.gov

Prof. D. K. Yoon
KAIST Institute for Nanocentury, Korea Advanced Institute of Science and Technology (KAIST), Daejeon 34141, Republic of Korea

†These authors contributed equally.

Keywords: cholesteric liquid crystal elastomer, mechanochromic, photonic crystal, optical rotation, visual signaling

Mechanochromic photonic materials present promising prospects for enhancing diverse facets of human life. Cholesteric liquid crystal elastomers (CLCEs) present immediate mechanochromic properties, allowing their utility in various fields, including camouflages, textiles, and anticounterfeiting. Nonetheless, it is essential to provide differentiated color information corresponding to diverse types and degrees of deformation for practical use in real life. Herein, we investigate the mechanochromic responses of CLCEs using their optical rotation under compression and uniaxial stretching. The CLCEs exhibit the same reflection colors indistinguishable for compression and uniaxial stretching due to their contracted pitches. In contrast, the linearly polarized light passing through deformed CLCEs can be modulated by optical rotation, resulting in distinct transmission colors that can be discerned through mechanical deformations. We demonstrate a visual signaling system with color information derived from optical rotation. By comprehending and manipulating the mechanoresponsive behavior of CLCEs, we can advance these materials into innovative solutions with enhanced functionality and performance, thereby broadening their applications for human life enhancement.

1. Introduction

Color signals are a prevalent mode of communication in nature, utilized by diverse organisms to convey information and interact with their environment and conspecifics.[1–4] Mechanochromic materials have the ability to bridge the gap between the artificial and natural realms by altering their colors in response to mechanical stimuli in a way that mimics living organisms.[5–9] In particular, mechanochromic photonic crystals (PCs), visualizing strain as a structural color change, are recently drawing great attention due to their potential for use in developing smart materials,[10–12] strain sensors,[13–19] and wearable industries.[20–22] The structural color variation of PCs in response to the mechanical deformation results from the modulated periodicity of regular nanostructures.[23,24] To realize an immediate response with respect to deformation, soft material-based PCs in the form of elastomers or gels have been developed,[25,26] showing fully reversible and dynamic color changes over the entire visible region.

Among various mechanochromic PC materials, cholesteric liquid crystal elastomers (CLCEs) emerge as a promising option. CLCEs feature self-assembled helical nanostructures comprising crosslinked networks with covalently bonded main chains, offering ease of processability and mechanical sensitivity.[27–31] The periodic nanostructures of the CLCEs with a well-defined helical pitch (p) exhibit vivid structural color, which is determined by the central

wavelength of the photonic bandgap, $\lambda_c = (n_e + n_o)\, p/2$, and bandwidth, $\Delta\lambda = (n_e - n_o)\, p$, where n_e and n_o are the extraordinary and ordinary refractive indices of liquid crystal (LC) molecule.[32–34] In this respect, innovative works have capitalized on the mechanochromic response of CLCEs across various domains, such as anticounterfeiting,[31,35] camouflages,[27,36] textiles,[29,37] and soft actuators.[38] Most prior studies, however, have demonstrated blue-shifted reflection colors that provide only one-dimensional information regarding the presence or absence of mechanical deformation, which is not significantly new from the mechanochromic demonstration using conventional PC elastomers.[25,38,39] Relying solely on the reflection colors for deformation lacks precision in conveying stress-related information and constrains effective color-based communication. This limitation might stem from the inability to fully harness the chiroptical properties derived from the helical structure of CLCEs. Given the active and dynamic nature of the real world, it becomes imperative to provide discernible color information corresponding to diverse types and degrees of deformation.

Some marine organisms, such as mantis shrimp, possess the ability to perceive visual signals produced by polarized light and employ them for conspecific communication (**Figure 1a**).[40,41] The patterns expressed through variations in angle or degree of polarization offer several advantages over other forms of visual information. For instance, color perception under ambient light can be influenced by environmental conditions, such as atmospheric disturbances or turbidity, leading to misinterpretation of the intended information by the recipient. Conversely, polarization information is less susceptible to such environmental perturbations than other visual dimensions,[40,42] thereby establishing its reliability and serving as a catalyst for innovative approaches to the use of polarization in color-based communication.

This paper presents an innovative integration of CLCEs with optical rotation in transmission mode, leveraging the inherent chirality of helical structures of CLCEs. We investigate the mechanochromic responses of CLCEs placed between polarizers under two different mechanical deformations: compression and uniaxial stretching. These deformations induce differing optical rotation characteristics due to changes in the helical structures. Specifically, compressed CLCE (C-CLCE) retains its helical structure, whereas stretched CLCE (S-CLCE) loses chirality by the uniaxial orientation of the main chains. Drawing on previous research regarding the manipulation of optical rotation in chiral PCs using cholesteric liquid crystal (CLC) film,[43,44] the linearly polarized light (LPL) passing through the deformed CLCE experiences varying optical rotation, exhibiting different colors for compression and uniaxial stretching. As a proof of concept, we develop a visual signaling system, showing different patterns or colors depending on the types and degrees of deformation. This finding will help

design new materials with tailored optical properties and mechanical functionalities for advanced optical applications such as strain sensors or soft robots.

2. Results and Discussion

2.1. Optical Rotation-Based Mechanochromic Response of CLCE

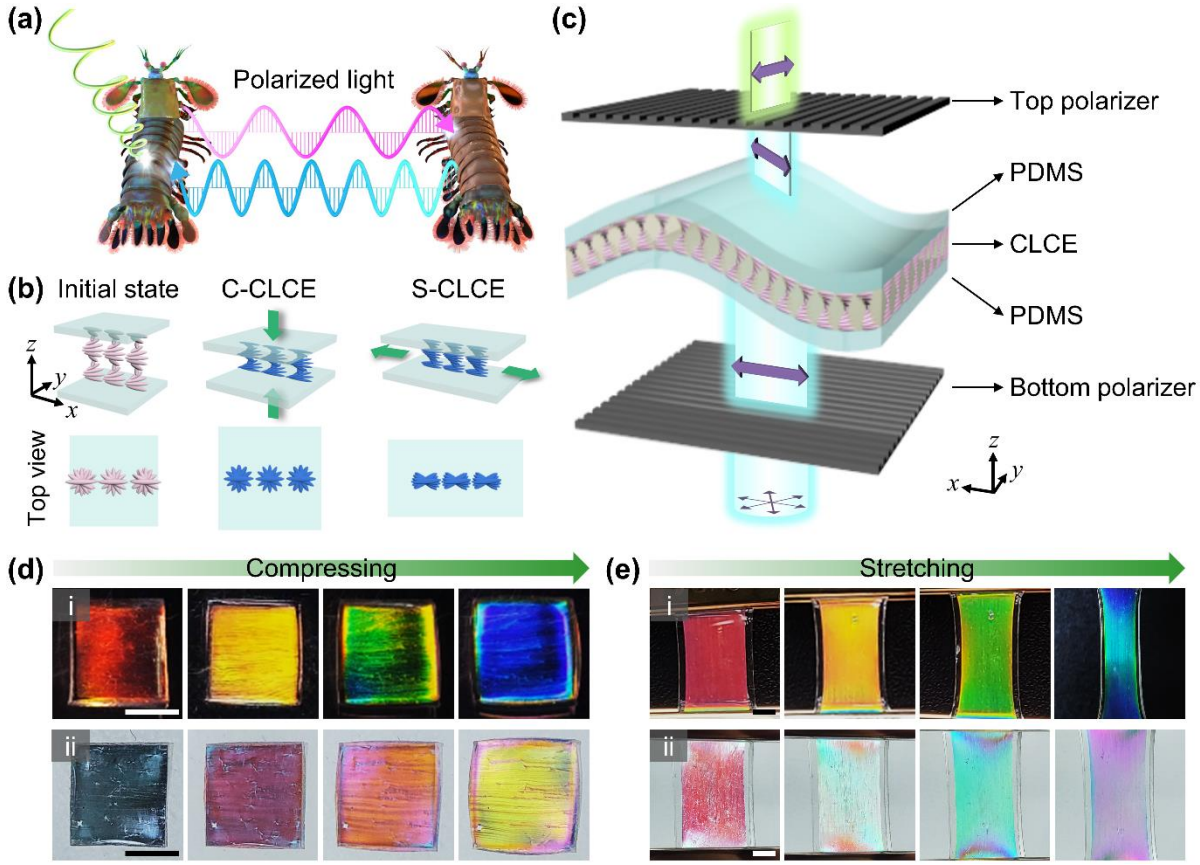

Figure 1. Optical rotation-based mechanochromic responses of cholesteric liquid crystal elastomer (CLCE). a) Illustration of mantis shrimp using polarized lights for conspecific communication. b) Schematic illustration of the macroscopic deformation of compressed CLCE (C-CLCE) and uniaxially stretched CLCE (S-CLCE). c) Schematic illustration of experimental system using a multi-layered CLCE sandwiched between elastic polydimethylsiloxane (PDMS) films. The backlight source passes through the bottom polarizer, multi-layered CLCE, and top polarizer in order. The purple arrow represents the polarization axis of incident linearly polarized light (LPL). d,e) Photographs of (d) C-CLCE and (e) S-CLCE in (i) reflection mode and (ii) transmission mode, respectively. Photographs in transmission mode are taken with two polarizers. All scale bars are 3 mm.

For soft elastic mechanical properties and a fast recovery process, a multi-layered CLCE film is prepared by sealing the freestanding CLCE with flexible polydimethylsiloxane (PDMS).

Incorporating PDMS as a supporting layer can effectively apply stress to CLCE and protect the film from damage, enabling a fully reversible mechanochromic response.[35,36] Upon subjecting the multi-layered CLCE film to compression and uniaxial stretching, distinct structural differences in the helical arrangement occur for each deformation scenario (Figure 1b). The strain along the helical axis, ε_z, during compression is defined as $\Delta l_z/l_z$, where l_z and Δl_z represent the initial and deformed lengths of the film, respectively. During uniaxial stretching, ε_z can be predicted by Hooke's law of transversely isotropic materials,[36,45,46]

$$\varepsilon_z = -\nu_2 \varepsilon_x \quad (1)$$

where Poisson's ratio ν_2 is the strain along the helical axis to the tensile strain, ε_x. Both compression and uniaxial stretching induce deformation along the thickness direction of CLCE film, resulting in changes in the p and λ_c of the CLCE.[47–49] However, C-CLCE undergoes isotropic deformation in the *xy* plane with only contraction along the *z*-axis and maintains the chirality of the nanostructure. On the other hand, S-CLCE experiences simultaneous anisotropic strain along *x*-, *y*-, and *z*-axes, eventually becoming uniaxially oriented along the stretching direction.

To investigate the optical rotation-based mechanochromic response of CLCEs, the backlight source transmits the bottom linear polarizer, multi-layered CLCE film, and the top linear polarizer in order (Figure 1c). After transmitting through the CLCE, the polarization axis of incident LPL rotates into a certain angle, β, which corresponds to optical rotation and can be described by the following equation:

$$\beta(\lambda) = \frac{\pi p \bar{n}^2}{4\lambda^2} \frac{d}{1-(\lambda/\lambda_c)^2} \quad (2)$$

where λ, $\bar{n}$, and d represent the incident wavelength of light, average refractive index in the CLCE, and film thickness, respectively.[50] Deforming CLCE films directly affects parameters determined by molecular alignment and structure, such as n, p, λ_c, and d. The intensity of the transmitted light through two linear polarizers and multi-layered CLCE film is governed by $\beta(\lambda)$ and the angle between two polarizers, θ, according to modified Malus' law, $I = I_0\cos^2(\theta + \beta(\lambda))$, where I_0 and I represent the intensities of the incident and transmitted LPL, respectively.[43,51,52] As a result, optical rotation-based transmission color variation can be achieved.[43] The mechanochromic responses originating from the deformed structures can only be distinguished in transmission mode, not reflection mode. In reflection mode (row (i) in Figure 1d,e), both C-CLCE and S-CLCE show the same color changes from red to blue with increasing strain (Movies S1 and S2). In contrast, in transmission mode with two linear polarizers (row (ii) in Figure 1d,e), they exhibit significantly different colors at $\theta = 50°$ as the strain increases, which can be explained by the optical rotation of the deformed CLC structures

(Movies S3 and S4). This color distinction on the deformations implies the feasibility of a visual signaling system with color information derived from polarized light.

2.2. CLCE Fabrication and Characterization

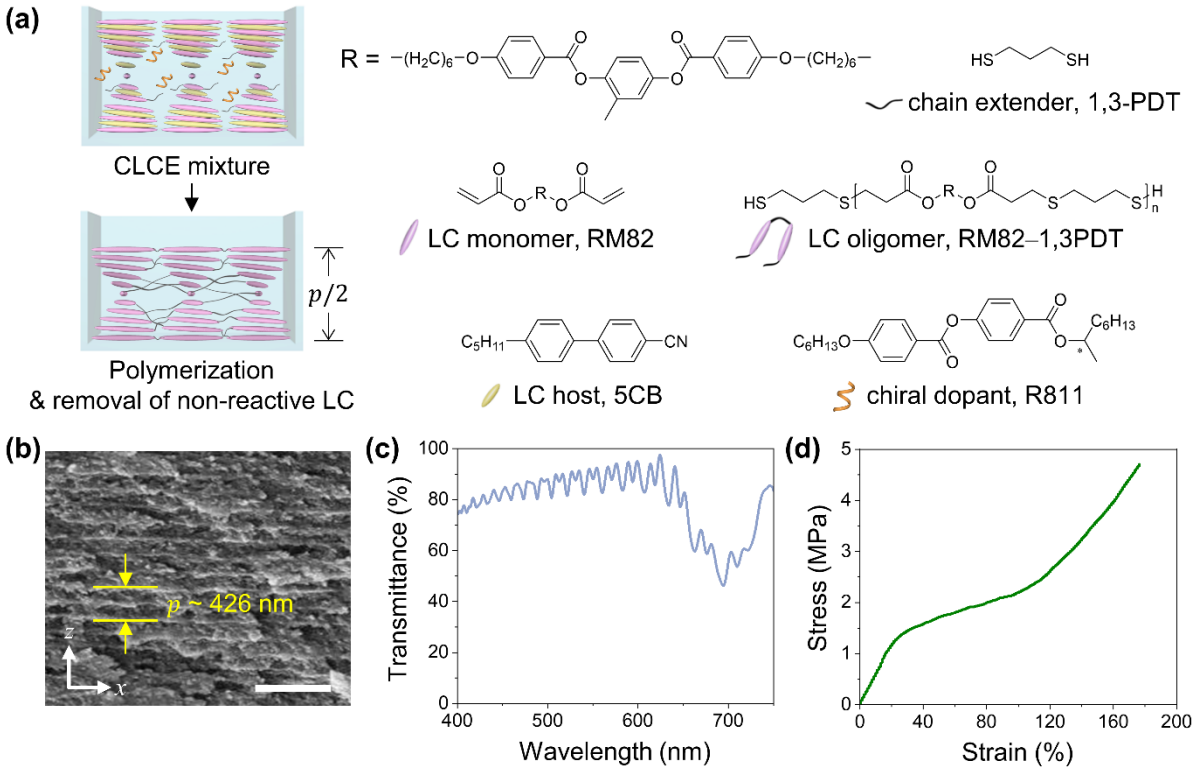

Figure 2. Fabrication of CLCE and its morphological, optical, and mechanical characteristics. a) Schematic illustration of the fabrication process for CLCE film and chemical structures of the compounds consisting of the CLCE mixture. *p* is helical pitch of resulting CLCE. b) Cross-sectional scanning electron microscopic (SEM) image of the CLCE, where *p* is 426 nm. Scale bar is 1 μm. c) Transmittance spectrum of the freestanding CLCE at initial state without applied strain. The initial central wavelength (λ_c) of photonic bandgap is 697 nm. d) Stress–strain curve of the CLCE under the application of uniaxial tensile strain.

Fabrication of the freestanding CLCE film is based on thiol–Michael addition reaction between acrylate-terminated LC monomer and thiol-terminated LC oligomer (see **Figure 2a**, Figure S1, and Methods for details). First, a mixture of CLCE consists of LC monomer, RM82, LC oligomer, RM82–1,3PDT, and non-reactive LC. The LC oligomer is synthesized by extending the chains of the LC monomer with a dithiol linker molecule via Michael addition reaction.[53] The non-reactive LC containing LC host, 5CB, and chiral dopant, R811, is used as a phase stabilizer by lowering the viscosity of monomers and oligomers and inducing the chiral nematic phase, which plays a role as a scaffold for the helical nanostructure. The CLCE mixture is

injected into polyvinyl alcohol (PVA)-coated sandwich cell by capillary force. After the UV-polymerization by thiol–acrylate click reaction, the non-reactive LC and unreacted residuals are removed for mechanical stability. The glass transition temperature, T_g, of the CLCE film is 4.0±5.8 ℃, confirmed by differential scanning calorimetry (DSC) measurements (Figure S2). Finally, a freestanding CLCE film is sandwiched between a pair of PDMS substrates, making a multi-layered CLCE film with remarkable elastic deformation. The cross-sectional scanning electron microscopic (SEM) image of the resulting CLCE film reveals periodic helical nanostructures with a p of 426 nm (Figure 2b). The transmittance spectrum presents the photonic bandgap in the visible region as a spectral dip with λ_c of 695 nm and $\Delta\lambda$ of 70 nm (Figure 2c). The transmittance of 2 mm-thick PDMS without CLCE averages 98.2±1.0% at 400–750 nm, which is transparent enough to assess the optical properties of the CLCE film (Figure S3). Young's modulus (E) of the freestanding CLCE film is 0.12 MPa from the stress–strain curve under tensile strain, ensuring good elasticity to investigate the mechanochromic response of CLCE (Figure 2d).

2.3. Optical Characteristics of CLCE under Mechanical Deformation

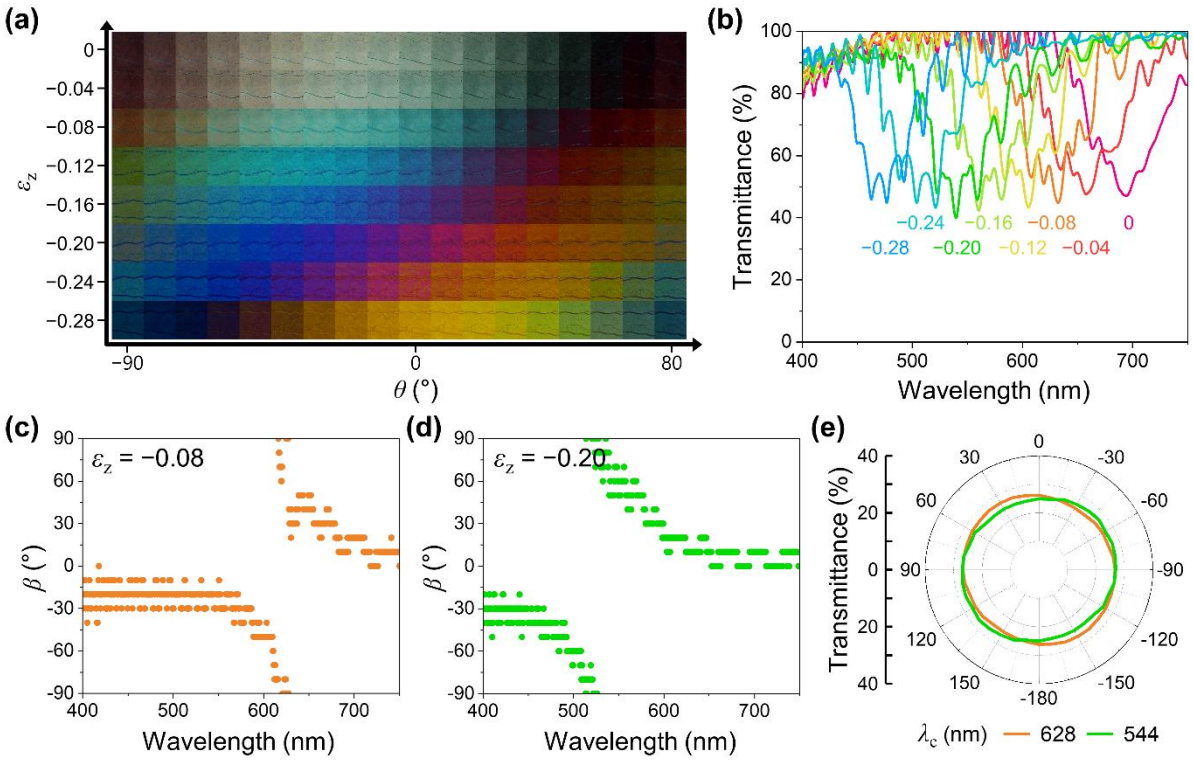

Figure 3. Mechanochromic response of C-CLCE film. a) Color palette consisting of optical rotation-based colors of C-CLCE. The x- and y-axes represent θ from −90° to 80° and ε_z, respectively. Each image size is 0.2 mm × 0.2 mm. b) Transmittance spectra of C-CLCE at

different ε_z values. c,d) Optical rotation of C-CLCE at (c) $\varepsilon_z = -0.08$ and (d) $\varepsilon_z = -0.20$. e) Polarization states of each λ_c of C-CLCE at $\varepsilon_z = -0.08$ and -0.20.

To compare the optical rotation-based mechanochromic responses with different deformations that are compression and stretching, the optical characteristics of C-CLCE film are investigated (**Figure 3**). The color palette is comprised of polarized optical microscopic (POM) images in transmission mode, taken while rotating the top polarizer with the C-CLCE placed between two polarizers (Figure 3a). The *x*- and *y*-axes represent θ from −90° to 80° and ε_z from 0 to −0.28, respectively. The combination of compressive strain and rotating a polarizer allows a wide range of transmission colors to be obtained with a single CLCE film.[43] Such a broad color variation has not previously been presented with typical elastomers based on PCs such as CLC, block copolymers, and colloidal particles. The transmittance spectra show the photonic bandgap with a shift in λ_c towards shorter wavelengths as ε_z increases while maintaining a constant transmittance of approximately 50% (Figure 3b and Table S1). In addition, as ε_z decreases, the $\Delta\lambda$ of the photonic bandgap decreases in the short range from 72 nm to 66 nm. The broad bandgaps in the measured transmittance imply the films have broad pitch distributions rather than well-defined pitches. It can be attributed to the intrinsic chemical structures of the CLCE films, which are composed of heterogeneity of materials and may possess porosity resulting from the non-reactive LC removal process. At $\varepsilon_z = -0.08$, the optical rotation flips the sign and diverges at the photonic bandgap with λ_c of 628 nm, which is a typical characteristic of chiral photonic crystals due to the optical resonance effect (Figure 3c).[54,55] Even with ε_z increasing to −0.20, the optical rotation shifts toward λ_c of 544 nm while maintaining a divergent configuration, indicating the preserved helical structure of CLCE under compressive stress (Figure 3d and Figure S4). When the transmittance is measured while rotating the top polarizer at ε_z of −0.08 and −0.20, the antisymmetric intensity modulation around λ_c is observed,[43] leading to the color variation of the C-CLCE depending on θ (Figure S5). Therefore, both the polarization states of transmitting λ_c at ε_z of −0.08 and −0.20 exhibit circular polarization by selective Bragg reflection (Figure 3e).[32,56]

Next, we examined the optical characteristics of the S-CLCE film (**Figure 4**). Similar to the C-CLCE, the S-CLCE demonstrates diverse colors depending on the combination of tensile strain and the polarizer rotation (Figure 4a). Notably, as the strain increases, the λ_c of the S-CLCE shifts toward shorter wavelengths, similar to the behavior observed in C-CLCE. However, the color palette of the S-CLCE markedly differs from that of the C-CLCE. Moreover, the transmittance spectra of the S-CLCE exhibit distinct trends in transmittance and $\Delta\lambda$

compared to the C-CLCE (Figure 4b and Table S2). Initially, the S-CLCE in its unstrained state shows a photonic bandgap with λ_c of 689 nm, $\Delta\lambda$ of 69 nm, and transmittance of 50% (state I). As the tensile strain increases, both the transmittance and $\Delta\lambda$ of the S-CLCE are drastically decreased and narrowed (state II). With further increases in tensile strain, the transmittance and $\Delta\lambda$ begin to increase and broaden once again (state III). In addition, the polarization states of the transmitted light at λ_c through the S-CLCE are measured at ε_z values of 0, −0.20, and −0.28 (Figure 4c–e). At ε_z = 0, the λ_c of 690 nm exhibits CPL by Bragg reflection, while other wavelengths show the rotating LPL resulting from the optical rotation (Figure 4c). As the strain increases to ε_z = −0.20, deformed CLC structure induces elliptical polarization for the λ_c of 543 nm and LPL with minimal rotation for other wavelengths (Figure 4d). At ε_z = −0.28, the polarization state of λ_c of 484 nm becomes LPL, and other wavelengths also remain as LPL with minimal rotation, similar to the case of ε_z = −0.20 (Figure 4e).

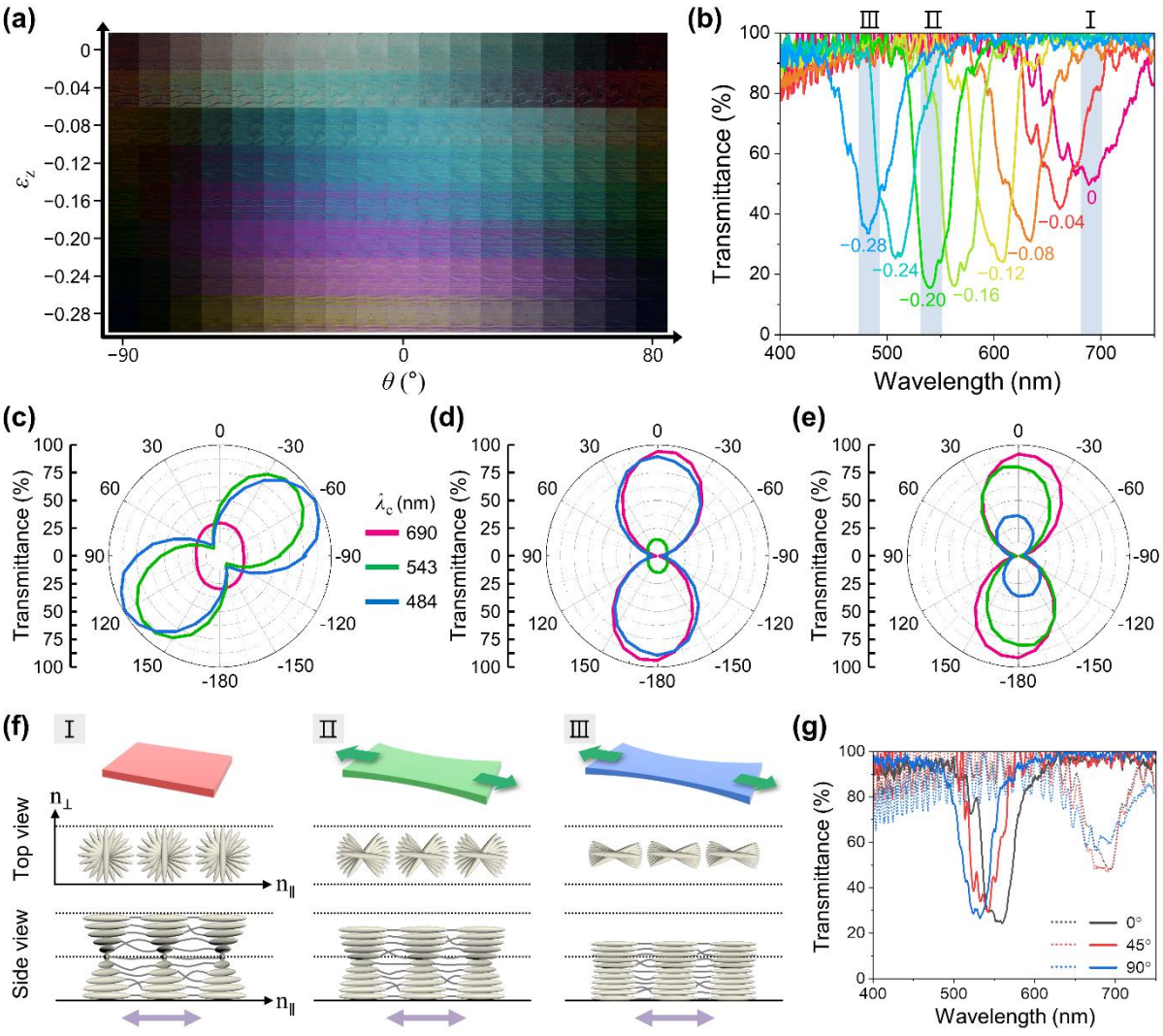

Figure 4. Mechanochromic response of S-CLCE film. a) Color palette consisting of optical rotation-based colors of S-CLCE. The *x*- and *y*-axes represent θ from −90° to 80° and ε_z,

respectively. Each image size is 0.1 mm × 0.1 mm. b) Transmittance spectra of S-CLCE at different ε_z values. c–e) Polarization states of λ_c at ε_z values of (c) 0, (d) −0.20, and (e) −0.28. f) Schematic illustration of macroscopic and microscopic deformation of S-CLCE at states I to III, marked on (b). The purple arrow represents the polarization axis of incident LPL, and $n_{\parallel}$ and $n_{\perp}$ represent the refractive index components parallel or perpendicular to the polarization axis of incident LPL, respectively. g) Transmittance of S-CLCE according to the rotation of sample stage. Black, red, and blue lines represent the angle of sample stage rotation of 0°, 45°, and 90°, respectively, and dashed and solid lines are for CLCE at the initial state and after uniaxially stretched, respectively. Here, the angle of 0° is when the uniaxial stretching direction is parallel to the polarization axis of incident LPL.

According to the measured transmittance and polarization states, the microscopic deformation of the S-CLCE from states I to III can be elucidated by considering the incident LPL and the molecular alignments (Figure 4f). In state I, the unstretched CLCE consists of periodic chiral structures made of birefringent molecules with n_e and n_o along the helical axis. This arrangement induces Bragg reflection only for CPL with the same handedness as the chiral structures.[32,56,57] Therefore, transmitted light through the CLCE shows a transmittance of 50% (Figure 4b), and the polarization state at λ_c is CPL with the opposite handedness to its chiral structures (Figure 4c). Moreover, the rotated LPL for the wavelengths out of the photonic bandgap means that the periodic chiral structures of the CLCE cause the optical rotation following Equation 2. Upon uniaxial stretching in state II, the thickness of the CLCE is shrunk, and the helical structures are deformed yet still periodic along the helical axis. Moreover, the molecules gradually align along the stretching direction, leading to the simultaneous loss of chirality in the S-CLCE. The incident LPL is still affected by the periodic refractive index modulation, which is smaller than the birefringence of the case of stage I, $n_e - n_o$, resulting in a narrow $\Delta\lambda$ of the Bragg reflection. In addition, due to the weak chirality of S-CLCE, the film reflects the incident LPL for the λ_c with a transmittance of less than 20% and transmits the light with minimal optical rotation, which is close to a phenomenon of non-chiral Bragg reflection.[30,38,58] Furthermore, the incident LPL experiences different refractive index modulations depending on the angle between the polarization direction and the stretching direction (Figure 4g): when the stretching direction is parallel (perpendicular) to the polarization direction of the incident LPL, light is affected by high (low) refractive indices around n_e (n_o). Therefore, when the angle is 0°, the λ_c has a longer wavelength than the case of the angle of 90°. Finally, with further strain in state III, most main chains of S-CLCE are

uniaxially oriented, leading to loss of the periodic refractive index modulation. Consequently, the Bragg resonant reflection becomes weak, which broadens the $\Delta\lambda$ of the photonic bandgap. The strong linear birefringence originating from the uniaxial main chains of S-CLCE contributes to the contrasting color palettes observed between S-CLCE and C-CLCE.

2.4. Structural Analysis of CLCE under Mechanical Deformation

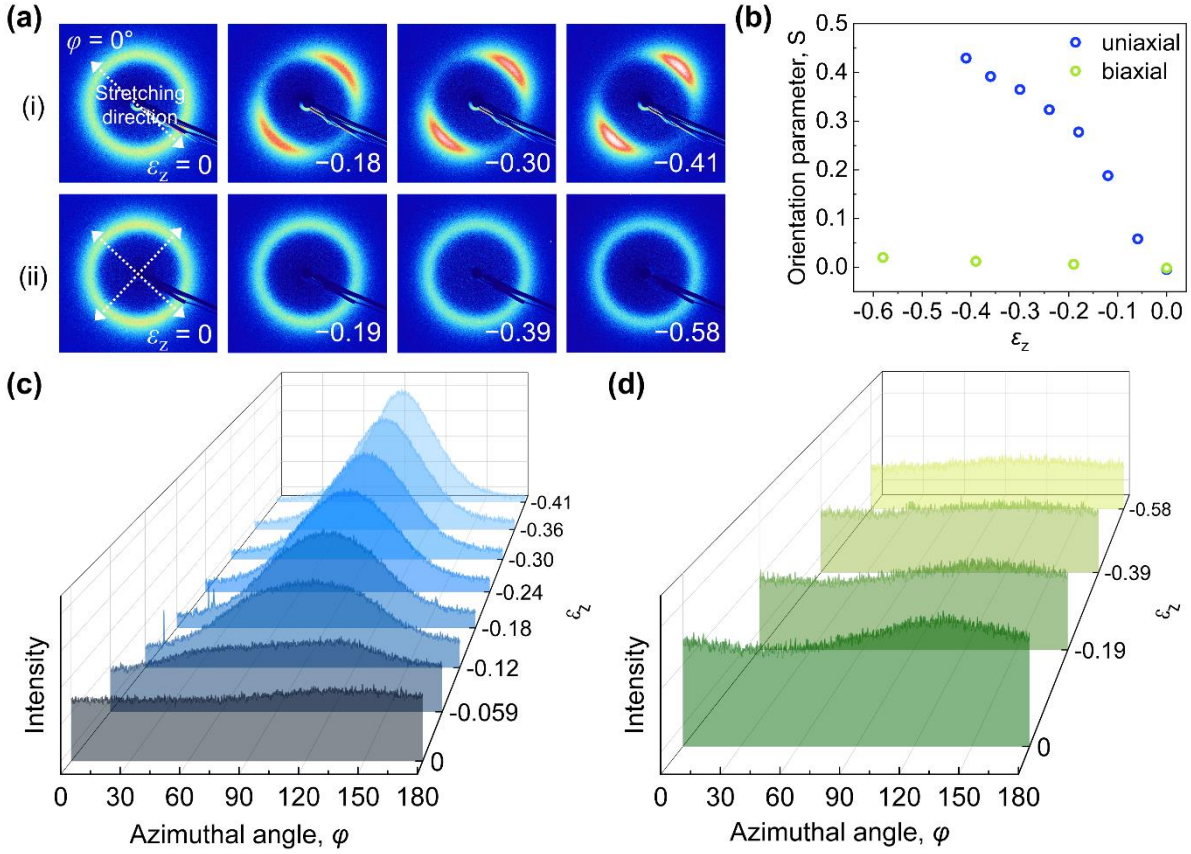

Figure 5. Structural analysis of freestanding CLCE according to uniaxial stretching and biaxial stretching. a) Two-dimensional X-ray diffraction images of CLCE being mechanically deformed by (i) uniaxial stretching and (ii) biaxial stretching at different ε_z values, respectively. Here, the uniaxial stretching direction is defined as the azimuthal angle, φ, of 0°. b) Plot of orientation parameter, S, of CLCE as a function of ε_z values. c,d) Azimuthal intensity profiles at q = 1.39 Å^{-1} of CLCE upon (c) uniaxial stretching and (d) biaxial stretching depending on ε_z values.

Using a freestanding CLCE film without the PDMS layers, we conducted wide-angle X-ray diffraction (WAXD) experiments in transmission mode with synchrotron radiation to directly show the structural difference between C-CLCE and S-CLCE (**Figure 5**). Due to the experimental constraints inherent in WAXD regarding the application of compression, biaxial

stretching was instead employed to CLCE using a customized tensile stage (Figure S6). The strain along the thickness direction upon biaxial stretching can be calculated by Equation 3, where Poisson's ratio v_1 is the strain along one of the principal axes to that along the other axis in the transverse plane.[36,45,46]

$$\varepsilon_z = -\frac{v_2}{1-v_1}\left(\varepsilon_x + \varepsilon_y\right) \quad (3)$$

We confirmed that biaxial stretching shows the same radial strain distribution as compression, although the strain in the transverse plane for biaxial stretching is slightly greater than that for compression (Figure S7). Thus, we predicted that the molecular arrangements in CLCE film under compression based on the findings from the biaxial stretching of CLCE, as compression data were unattainable through WAXD experiment in transmission mode.

The chain orientations of CLCE upon uniaxial and biaxial stretching are evaluated through two-dimensional WAXD patterns (row (i) and row (ii) in Figure 5a, respectively). At the initial state, the diffraction peak at q = 1.39 Å^{-1} shows the isotropic distribution for both uniaxial and biaxial stretching (Figure 5a and Figure S8). As the ε_z increases, however, CLCE upon uniaxial stretching shows a strong anisotropic pattern localized perpendicular to the stretching direction. In contrast, CLCE under biaxial stretching remains a radial distribution without angle dependence. The degree of orientation is quantitatively analyzed using the Hermans orientation parameter, *S*, calculated from azimuthal intensity profiles (see Figure 5b and Methods for details). The peak intensities at q = 1.39 Å^{-1} with respective to the azimuthal angle are plotted for both uniaxial and biaxial stretching (Figure 5c,d, respectively). We obtain $S \approx 0$ for biaxial stretching regardless of strain, representing a low anisotropy along the transverse plane of CLCE. In contrast, the orientation parameter increases with uniaxial stretching, reaching a value of 0.43 at $\varepsilon_z = -0.41$, indicating that the main chains of CLCE are well oriented along the stretching direction. These findings support our assertion that the helical nanostructures of CLCE undergo different deformations depending on the nature of the mechanical force.

2.5. Visual Signaling with Color Information Derived from Optical Rotation

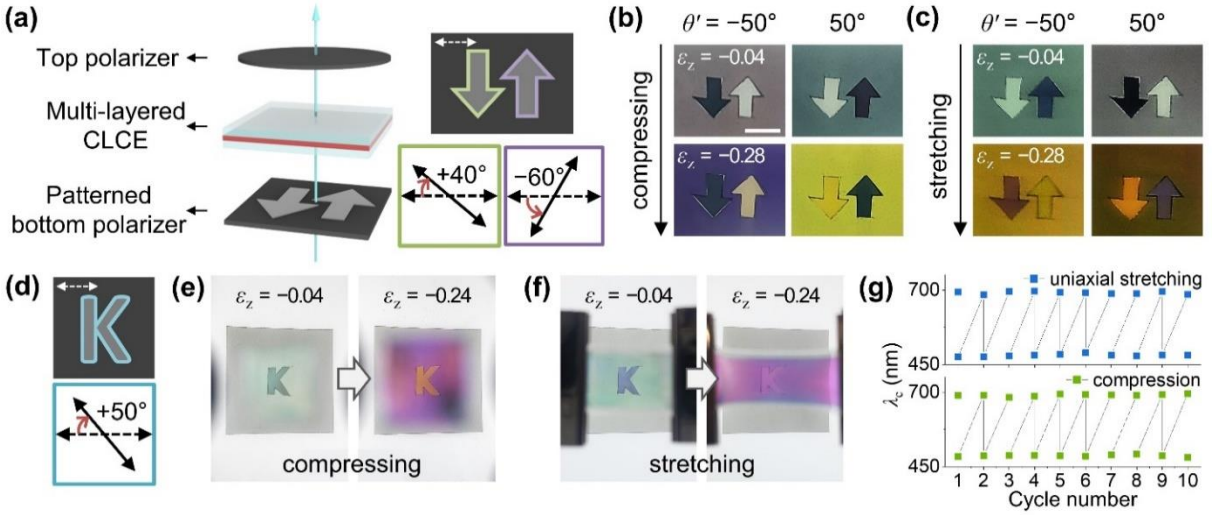

Figure 6. Visual signaling that is discernible according to the types and degrees of deformation. (a) Schematic of the experimental setup with the patterned bottom polarizer. The dashed and solid arrows indicate the polarization axis of the background and patterns, respectively. Here, θ' is the angle between the polarization axis of the background of the bottom polarizer and that of the top polarizer. (b, c) Photographs of (b) C-CLCE and (c) S-CLCE at ε_z values of −0.04 and −0.28 using the top polarizer with θ' set at −50° and 50°. Scale bar is 10 mm. (d) "K"-patterned bottom polarizer. (e, f) Photographs of (e) C-CLCE and (f) S-CLCE at ε_z values of −0.04 and −0.24 using the top polarizer with θ' set at −30°. (g) Reversibility of λ_c of S-CLCE (blue dots) and C-CLCE (green dots) by alternating ε_z values of 0 and −0.28.

Based on the distinctive optical rotation characteristics associated with mechanical deformations, we developed a visual signaling system that offers discernible color information specific to deformation (**Figure 6**). In order to convey different information for compression and uniaxial stretching, we employed a patterned bottom polarizer with varied polarization axes (Figure 6a). The polarization axes of the downward and upward arrow patterns on the bottom polarizer are deviated from that of the background by +40° and −60°, respectively (Figure S9). The visual signals can be obtained by placing the multi-layered CLCE between the top polarizer and patterned bottom polarizer and adjusting θ', defined as the angle between the polarization axis of the top polarizer and that of the background of the bottom polarizer. The color information at each pattern arises from distinct optical rotations depending on the predetermined angle of the incident LPL. At a slight deformation of $\varepsilon_z = -0.04$, both downward and upward arrows are distinguishable for C-CLCE and S-CLCE, exhibiting different colors depending on θ' (Figure 6b,c). However, as the strain increases to −0.28, the upward arrow is more emphasized for C-CLCE against the background, while the downward arrow is more

clearly visible for S-CLCE (Movies S5 and S6). The color difference between the background and particular arrow gradually diminishes, ultimately rendering only one arrow clearly visible at specific θ'. When the bottom polarizer is patterned as "K" with its polarization axis deviating from that of the background by +50°, and the angle θ' is set at −30°, the resulting pattern gives asymmetric information for compression and uniaxial stretching (Figure 6d). The "K" pattern consistently retains distinct visibility for C-CLCE as strain increases from −0.04 to −0.24 (Figure 6e), while its visibility diminishes for S-CLCE (Figure 6f). This distinctive behavior renders it functional as a strain-induced watermark or camouflage patterns, facilitating the visualization of the nature of deformations. Notably, despite having the same values of ε_z and θ', C-CLCE and S-CLCE show entirely dissimilar color information for the same pattern. This system is fully reversible and provides reliable information even during repetitive operation, as demonstrated by the recovery of λ_c of the CLCE under mechanical deformation during the cycling test alternating $\varepsilon_z = 0$ and −0.28 (Figure 6g). We emphasize that our visual signaling system, which has not been reported previously, is capable of providing accurate stress-related information, enabling effective color-based communication by exploiting the optical rotation characteristics of deformed CLCE.

3. Conclusion

In this paper, we have explored the mechanochromic responses of CLCE under compression and uniaxial stretching, highlighting their optical rotation characteristics arising from the deformed helical structures of CLCEs. Compression results in a well-maintained helical structure, while stretching leads to anisotropic strain and the loss of chirality. The unique optical properties of C-CLCE and S-CLCE, attributed to optical rotation, provide precise stress-related information through colors, which has not been reported in conventional mechanochromic PCs. By leveraging the distinctive optical properties, we have successfully demonstrated visual signaling capable of discerning the types and degrees of deformation. This system exhibits different colors or patterns depending on the mechanical deformation or the angle of the polarizer. The optical rotation-based mechanochromic responses of CLCE, harnessed in our visual signaling system, establish a solid foundation for a new avenue in the application of CLCE. We anticipate that employing sophisticated patterning technology will enable the realization of visual communication encompassing color information within more intricate and detailed patterns.

4. Methods

Materials: 1,3-propanedithiol (>99%, 1,3-PDT), 2,2-dimethoxy-2-phenylacetophenone (DMPA), 1,8-diazabicyclo[5.4.0]undec-7-ene (98%, DBU), poly(vinyl alcohol) (PVA, M_w 31,000–50,000, 98–99% hydrolyzed) were purchased from Sigma Aldrich. Butylated hydroxytoluene (analytical standard, BHT) was purchased from Tokyo Chemical Industry. Hydrochloric acid (HCl, 36.5% to 38.0%), dichloromethane (DCM), and ethanol were purchased from Duksan Pure Chemicals. Magnesium sulfate ($MgSO_4$, anhydrous powder) was purchased from Samchun Chemicals. 1,4-bis-[4-(6-acryloyloxy-hexyloxy)benzoyloxy]-2-methylbenzene (RM82) and 4-cyano-4-pentylbiphenyl (5CB) were purchased from Henan Wentao Chemical Product, (R)-2-octyl 4-[4-(hexyloxy)benzoyloxy]benzoate (R811) was purchased from Nanjing Aocheng Chemical, and polydimethylsiloxane (PDMS) was purchased from Dowhitech. All materials were used as supplied without further purification.

Preparation of CLCE mixture: LC oligomer, RM82–1,3PDT, was first synthesized via thiol–acrylate Michael addition between RM82 and 1,3-PDT.[53] The initial CLCE mixture consisted of 29 wt% RM82–1,3PDT, 22 wt% RM82, 34 wt% 5CB, 13wt% R811, 2 wt% DMPA as a photoinitiator, and 0.3 wt% BHT as an inhibitor for thermal polymerization. All chemical components were dissolved in DCM to mix homogeneously, and then DCM was completely evaporated under magnetic stirring at 100 °C for a few hours.

Preparation of multi-layered CLCE film: Slide glasses were bar-coated with 1 wt% PVA aqueous solution, followed by baking at 120 °C for 1 h. The sandwich cell was made of two PVA-coated glasses, and its gap was controlled using silica particles of ~30 μm in diameter. Then, the CLCE mixture was injected into the sandwich cell by capillary force and polymerized using 365 nm UV light (Ushio Shenzhen Inc.) with an effective power density of 10 mW cm^{-2} for 15 min. The sandwich cell filled with the CLCE mixture was manually disassembled by dissolving the PVA layer in deionized water, and the freestanding CLCE film was obtained. To remove the LC solvent composed of 5CB and R811 and any unreacted residuals, the freestanding CLCE film was immersed in ethanol for 24 h and completely dried at room temperature. The PDMS mixture (19:1 w/w of base and curing agent) was stirred for 5 min and cured at 70 °C for 2 h. The dried CLCE film was sealed with a pair of PDMS and then cured at 70 °C for 2 h, forming a multi-layered CLCE film. Each bottom and top PDMS layer have a thickness of ~1 mm.

Characterization: The phase transition temperature of the CLCE film was measured by DSC measurement (Diamond, PerkinElmer) operated from −50 to 220 °C at a heating/cooling rate of 10 °C min^{-1} under N_2 atmosphere. Optical textures of CLCEs were obtained using an upright polarized optical microscope (Nikon Eclipse LV100 POL) equipped with DS-Ri1 multicolor

camera (Nikon Instruments) in transmission mode. Photographs and videos were taken with a smartphone (Galaxy Z Flip 3, Samsung Electronics). The *p* of freestanding CLCE film was confirmed by cross-sectional SEM (MIRA3, TESCAN) at 3 kV and 310 μA. The mechanical properties of freestanding CLCE film were tested using universal testing machine (H1KT machine, Tinius Olsen). Transmittance and optical rotation were measured using a UV-vis-NIR spectrometer (USB2000+, Ocean Optics). Compression and uniaxial stretching were applied to the multi-layered CLCE film using customized transparent acrylic boards and a tensile testing stage (TST350, Linkam Scientific Instruments), respectively. WAXD experiments were conducted using a customized stage in transmission mode at the 9A U-SAXS beamline in Pohang Accelerator Laboratory. The wavelength and energy of the X-ray were 1.1179 Å and 11.09 keV, respectively, and the sample-to-detector distance was 0.2 m.

Optical measurement: Transmittance spectra in Figures 2c, 3b, 4b and 4g were normalized to that of a 2mm-thick PDMS film with incident LPL. Transmittance spectra in Figures 3e and 4c–e were normalized by the transmittance of the two parallel polarizers with a 2mm-thick PDMS film. The position of λ_c, $\Delta\lambda$, and transmittance at λ_c were determined by fitting a Gaussian function to each transmission peak in the raw data. Optical rotation was obtained by placing the CLCE film between two polarizers and measuring the transmittance while rotating the top polarizer from 0° to 180° at intervals of 10°. The optical rotation is defined as the angle at which the transmittance of each λ is maximized.

Calculation of Hermans orientation parameter: Diffraction intensities for the azimuthal angle, $I(\varphi)$, were recorded at q = 1.39 Å^{-1}, which corresponds to an average interchain distance of d = 4.5 Å, a typical value for nematic liquid crystals. The Hermans orientation parameter, S, was determined from $I(\varphi)$ using Equations 4–6.

$$S = \frac{1}{2}\{3(\cos^2\gamma) - 1\} \quad (4)$$

$$\cos^2\gamma = 1 - 2(\cos^2\varphi) \quad (5)$$

$$\cos^2\varphi = \frac{\int_0^{\pi} I(\varphi)\cos^2\varphi \sin\varphi d\varphi}{\int_0^{\pi} I(\varphi)\sin\varphi d\varphi} \quad (6)$$

Here, azimuthal angle φ represents the directional angle relative to the uniaxial stretching direction, which is defined as φ = 0° in this measurement.

Supporting Information

Supporting Information is available from the Wiley Online Library or from the author.

Acknowledgements

H.P. and H. J. L. contributed equally to this work. This study was supported by the National Research Foundation of Korea (2021R1F1A1047516, 2021M3C1C3097646, and 2018R1A5A1025208). This work was performed, in part, at the Center for Integrated Nanotechnologies, an Office of Science User Facility operated for the U.S. Department of Energy (DOE) Office of Science. Los Alamos National Laboratory, an affirmative action equal opportunity employer, is managed by Triad National Security, LLC for the U.S. Department of Energy's NNSA, under contract 89233218CNA000001. We gratefully acknowledge Dr. Young-Joo Lee for conducting the simulations and the support from Pohang Accelerator Laboratory in South Korea for using the 9A beamline.

Received: ((will be filled in by the editorial staff))
Revised: ((will be filled in by the editorial staff))
Published online: ((will be filled in by the editorial staff))

References

[1] I. C. Cuthill, W. L. Allen, K. Arbuckle, B. Caspers, G. Chaplin, M. E. Hauber, G. E. Hill, N. G. Jablonski, C. D. Jiggins, A. Kelber, J. Mappes, J. Marshall, R. Merrill, D. Osorio, R. Prum, N. W. Roberts, A. Roulin, H. M. Rowland, T. N. Sherratt, J. Skelhorn, M. P. Speed, M. Stevens, M. C. Stoddard, D. Stuart-Fox, L. Talas, E. Tibbetts, T. Caro, *Science* **2017**, *357*, DOI 10.1126/science.aan0221.

[2] J. Teyssier, S. V. Saenko, D. van der Marel, M. C. Milinkovitch, *Nat. Commun.* **2015**, *6*, 6368.

[3] D. Stuart-Fox, L. Ospina-Rozo, L. Ng, A. M. Franklin, *Trends Ecol. Evol.* **2021**, *36*, 187.

[4] T. L. Williams, S. L. Senft, J. Yeo, F. J. Martín-Martínez, A. M. Kuzirian, C. A. Martin, C. W. DiBona, C. T. Chen, S. R. Dinneen, H. T. Nguyen, C. M. Gomes, J. J. C. Rosenthal, M. D. MacManes, F. Chu, M. J. Buehler, R. T. Hanlon, L. F. Deravi, *Nat. Commun.* **2019**, *10*, 1.

[5] C. Li, Q. He, Y. Wang, Z. Wang, Z. Wang, R. Annapooranan, M. I. Latz, S. Cai, *Nat. Commun.* **2022**, *13*, 3914.

[6] D. A. Davis, A. Hamilton, J. Yang, L. D. Cremar, D. Van Gough, S. L. Potisek, M. T. Ong, P. V. Braun, T. J. Martínez, S. R. White, J. S. Moore, N. R. Sottos, *Nature* **2009**, *459*, 68.

[7] A. Lavrenova, D. W. R. Balkenende, Y. Sagara, S. Schrettl, Y. C. Simon, C. Weder, *J.*

Am. Chem. Soc. **2017**, *139*, 4302.

[8] G. Giordano, M. Gagliardi, Y. Huan, M. Carlotti, A. Mariani, A. Menciassi, E. Sinibaldi, B. Mazzolai, *Adv. Sci.* **2021**, *8*, 2100418.

[9] S. Zeng, D. Zhang, W. Huang, Z. Wang, S. G. Freire, X. Yu, A. T. Smith, E. Y. Huang, H. Nguon, L. Sun, *Nat. Commun.* **2016**, *7*, 11802.

[10] P. Güell-Grau, P. Escudero, F. G. Perdikos, J. F. López-Barbera, C. Pascual-Izarra, R. Villa, J. Nogués, B. Sepúlveda, M. Alvarez, *ACS Appl. Mater. Interfaces* **2021**, *13*, 47871.

[11] P. Wu, X. Shen, C. G. Schäfer, J. Pan, J. Guo, C. Wang, *Nanoscale* **2019**, *11*, 20015.

[12] D. Yang, Y. Hu, D. Ma, J. Ge, S. Huang, *Research* **2022**, *2022*, DOI 10.34133/2022/9838071.

[13] R. Zhao, Y. He, Y. He, Z. Li, M. Chen, N. Zhou, G. Tao, C. Hou, *ACS Appl. Mater. Interfaces* **2023**, *15*, 16063.

[14] T. H. Park, S. Yu, S. H. Cho, H. S. Kang, Y. Kim, M. J. Kim, H. Eoh, C. Park, B. Jeong, S. W. Lee, D. Y. Ryu, J. Huh, C. Park, *NPG Asia Mater.* **2018**, *10*, 328.

[15] I. Jurewicz, A. A. K. King, R. Shanker, M. J. Large, R. J. Smith, R. Maspero, S. P. Ogilvie, J. Scheerder, J. Han, C. Backes, J. M. Razal, M. Florescu, J. L. Keddie, J. N. Coleman, A. B. Dalton, *Adv. Funct. Mater.* **2020**, *30*, 2002473.

[16] P. Snapp, P. Kang, J. Leem, S. Nam, *Adv. Funct. Mater.* **2019**, *29*, 1902216.

[17] J. Chen, L. Xu, M. Yang, X. Chen, X. Chen, W. Hong, *Chem. Mater.* **2019**, *31*, 8918.

[18] D. Yang, S. Ye, J. Ge, *Adv. Funct. Mater.* **2014**, *24*, 3197.

[19] Z. Zhang, Z. Chen, Y. Wang, Y. Zhao, *Proc. Natl. Acad. Sci.* **2020**, *117*, 18310.

[20] Y. Guan, H. Li, S. Zhang, W. Niu, *Adv. Funct. Mater.* **2023**, *33*, 1.

[21] Q. Li, S. Liu, J. Wang, N. Mondele Mbola, Z. Meng, X. Wang, M. Xue, *J. Mater. Chem. C* **2022**, *10*, 9025.

[22] H. Liu, Y. Wang, Z. Shi, D. Tan, X. Yang, L. Xiong, G. Li, Y. Lei, L. Xue, *Small Methods* **2022**, *6*, 1.

[23] J. M. Clough, C. Weder, S. Schrettl, *Macromol. Rapid Commun.* **2021**, *42*, 2000528.

[24] R. Zhang, Q. Wang, X. Zheng, *J. Mater. Chem. C* **2018**, *6*, 3182.

[25] G. Chen, W. Hong, *Adv. Opt. Mater.* **2020**, *8*, 2000984.

[26] J. H. Shin, J. Y. Park, S. H. Han, Y. H. Lee, J. Sun, S. S. Choi, *Adv. Sci.* **2022**, *9*, 2202897.

[27] A. M. Martinez, M. K. McBride, T. J. White, C. N. Bowman, *Adv. Funct. Mater.* **2020**, *30*, 2003150.

[28] P. Zhang, G. Zhou, L. T. Haan, A. P. H. J. Schenning, *Adv. Funct. Mater.* **2021**, *31*, 2007887.

[29] Y. Geng, R. Kizhakidathazhath, J. P. F. Lagerwall, *Nat. Mater.* **2022**, *21*, 1441.

[30] R. Kizhakidathazhath, Y. Geng, V. S. R. Jampani, C. Charni, A. Sharma, J. P. F. Lagerwall, *Adv. Funct. Mater.* **2020**, *30*, 1909537.

[31] S. Hussain, S. Park, *ACS Appl. Mater. Interfaces* **2021**, *13*, 59275.

[32] M. Mitov, *Adv. Mater.* **2012**, *24*, 6260.

[33] D.-Y. Kim, C. Nah, S.-W. Kang, S. H. Lee, K. M. Lee, T. J. White, K.-U. Jeong, *ACS Nano* **2016**, *10*, 9570.

[34] D. Wang, S. Nam, W. Jung, H. J. Yang, S. S. Choi, *Adv. Opt. Mater.* **2023**, *11*, DOI 10.1002/adom.202202906.

[35] P. Zhang, X. Shi, A. P. H. J. Schenning, G. Zhou, L. T. Haan, *Adv. Mater. Interfaces* **2020**, *7*, 1901878.

[36] S.-U. Kim, Y.-J. Lee, J. Liu, D. S. Kim, H. Wang, S. Yang, *Nat. Mater.* **2022**, *21*, 41.

[37] Y. Geng, J. P. F. Lagerwall, *Adv. Sci.* **2023**, *2301414*, 1.

[38] J. Ma, Y. Yang, C. Valenzuela, X. Zhang, L. Wang, W. Feng, *Angew. Chemie Int. Ed.* **2022**, *61*, DOI 10.1002/anie.202116219.

[39] C. Kwon, S. Nam, S. H. Han, S. S. Choi, *Adv. Funct. Mater.* **2023**, *2304506*, 1.

[40] I. M. Daly, M. J. How, J. C. Partridge, S. E. Temple, N. J. Marshall, T. W. Cronin, N. W. Roberts, *Nat. Commun.* **2016**, *7*, 12140.

[41] T. W. Cronin, T.-H. Chiou, R. L. Caldwell, N. Roberts, J. Marshall, in *Polariz. Sci. Remote Sens. IV* (Eds.: J.A. Shaw, J.S. Tyo), **2009**, p. 74610C.

[42] Y. L. Gagnon, R. M. Templin, M. J. How, N. J. Marshall, *Curr. Biol.* **2015**, *25*, 3074.

[43] W. Park, H. Park, Y.-S. Choi, D. K. Yoon, *Adv. Opt. Mater.* **2022**, *10*, 2201099.

[44] S. Liu, L. Zhu, Y. Zhang, W. Chen, D. Zhu, P. Chen, Y. Lu, *Adv. Mater.* **2023**, *35*, DOI 10.1002/adma.202301714.

[45] R. A. Eubanks, E. Sternberg, *J. Ration. Mech. Anal.* **1954**, *3*, 89.

[46] W. C. Han, Y. Lee, S. Kim, H. J. Lee, Y. Kim, D. S. Kim, *Small* **2023**, *19*, 2206299.

[47] P. Cicuta, A. R. Tajbakhsh, E. M. Terentjev, *Phys. Rev. E* **2004**, *70*, 011703.

[48] M. Warner, E. M. Terentjev, R. B. Meyer, Y. Mao, *Phys. Rev. Lett.* **2000**, *85*, 2320.

[49] Y. Mao, E. M. Terentjev, M. Warner, *Phys. Rev. E* **2001**, *64*, 041803.

[50] H. de Vries, *Acta Crystallogr.* **1951**, *4*, 219.

[51] G. Park, H. Park, J. M. Wolska, J. G. Park, D. K. Yoon, *Mater. Horizons* **2022**, *9*, 2542.

[52] W. Park, T. Ha, T. S. Jung, K. I. Sim, J. H. Kim, J. M. Wolska, D. Pociecha, E. Gorecka, T. T. Kim, D. K. Yoon, *Nanoscale* **2020**, *12*, 21629.

[53] Y. Xia, X. Zhang, S. Yang, *Angew. Chemie Int. Ed.* **2018**, *57*, 5665.

[54] S. Chandrasekhar, K. N. S. Rao, *Acta Crystallogr. Sect. A* **1968**, *24*, 445.

[55] S. Chandrasekhar, J. S. Prasad, *Mol. Cryst. Liq. Cryst.* **1971**, *14*, 115.

[56] H. Kitzerow, C. Bahr, *Chirality in Liquid Crystals*, Springer-Verlag, New York, **2001**.

[57] L. Zhu, C.-T. Xu, P. Chen, Y.-H. Zhang, S.-J. Liu, Q.-M. Chen, S.-J. Ge, W. Hu, Y.-Q. Lu, *Light Sci. Appl.* **2022**, *11*, 135.

[58] C. L. C. Chan, M. M. Bay, G. Jacucci, R. Vadrucci, C. A. Williams, G. T. de Kerkhof, R. M. Parker, K. Vynck, B. Frka-Petesic, S. Vignolini, *Adv. Mater.* **2019**, *31*, 1905151.

Optical rotation-based mechanochromic responses of cholesteric liquid crystal elastomers are demonstrated under compression and uniaxial stretching. Compression allows for the well-maintained helical structure, whereas stretching induces anisotropic strain and a loss of chirality. A visual signaling system, utilizing optical rotation-based mechanochromic responses, provides discernible color information depending on the types and degrees of deformation.

H. Park†, H. J. Lee†, H. Ahn, W. C. Han, H. S. Yun, Y.-S. Choi*, D. S. Kim*and D. K. Yoon*

Mechanochromic Palettes of Cholesteric Liquid Crystal Elastomers for Visual Signaling

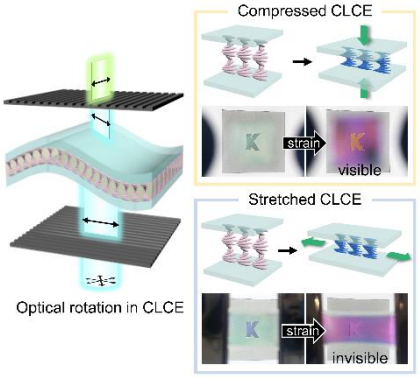

Supporting Information

Mechanochromic Palettes of Cholesteric Liquid Crystal Elastomers for Visual Signaling

Hyewon Park†, Hye Joo Lee†, Hyungju Ahn, Woong Chan Han, Hee Seong Yun, Yun-Seok Choi, Dae Seok Kim*and Dong Ki Yoon**

This file includes

Figures S1–S9

Tables S1, S2

Captions for Movies S1–S6

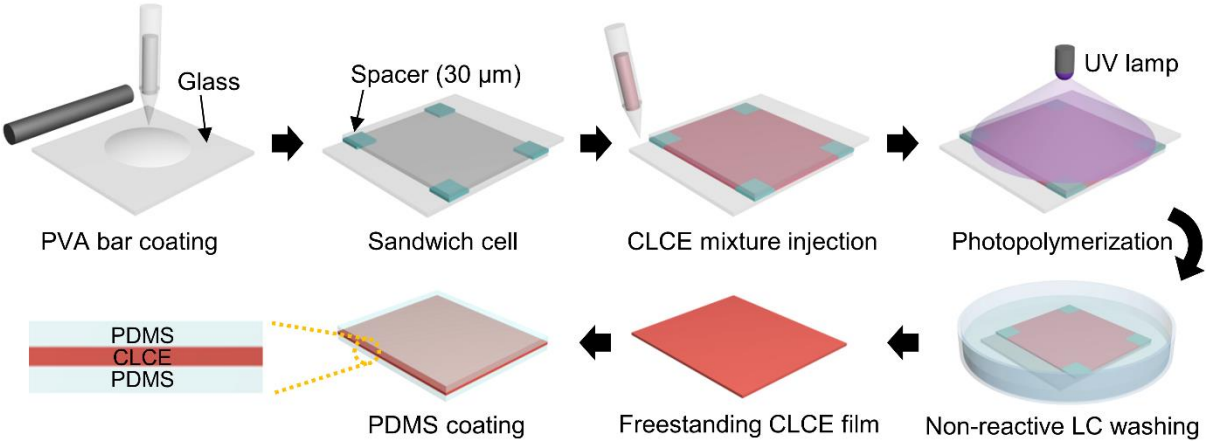

Figure S1. Schematic illustration of the fabrication process for multi-layered CLCE film.

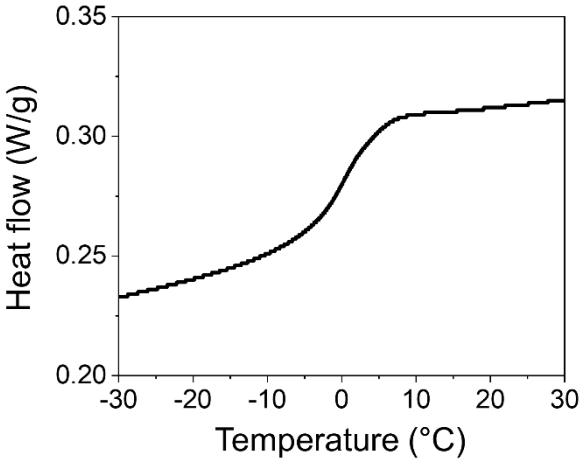

Figure S2. DSC 2nd heating thermograms of CLCE. The glass transition temperature, T_g, of the CLCE film is 4.0±5.8 ℃.

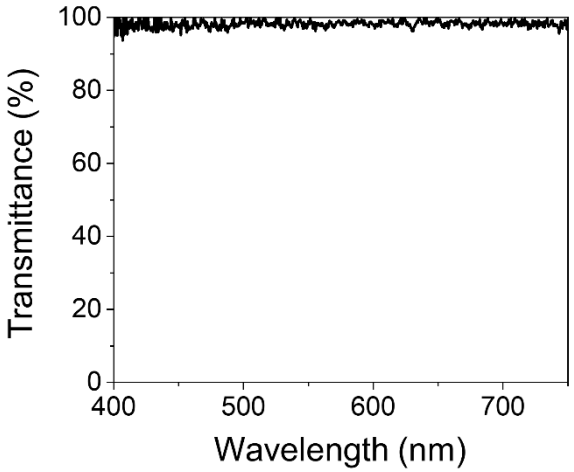

Figure S3. Transmittance spectrum of 2 mm-thick PDMS. The average transmittance of PDMS in 400–750 nm region is 98.2±1.0%. The transmittance is measured with incident LPL.

Table S1. Summary of optical characteristics, including position of λ_c, bandwidth $\Delta\lambda$, and the transmittance at λ_c for each C-CLCE.

ε_z	λ_c (nm)	$\Delta\lambda$ (nm)	Transmittance at λ_c (%)
0	695.4	72.2±0.9	50.0
−0.04	658.4	76.4±1.1	51.0
−0.08	628.0	63.8±1.0	50.5
−0.12	603.0	66.0±1.0	50.3
−0.16	572.3	68.4±1.0	50.5
−0.20	544.9	68.6±1.0	48.1
−0.24	510.6	68.2±1.0	50.3
−0.28	486.0	65.9±1.0	51.2

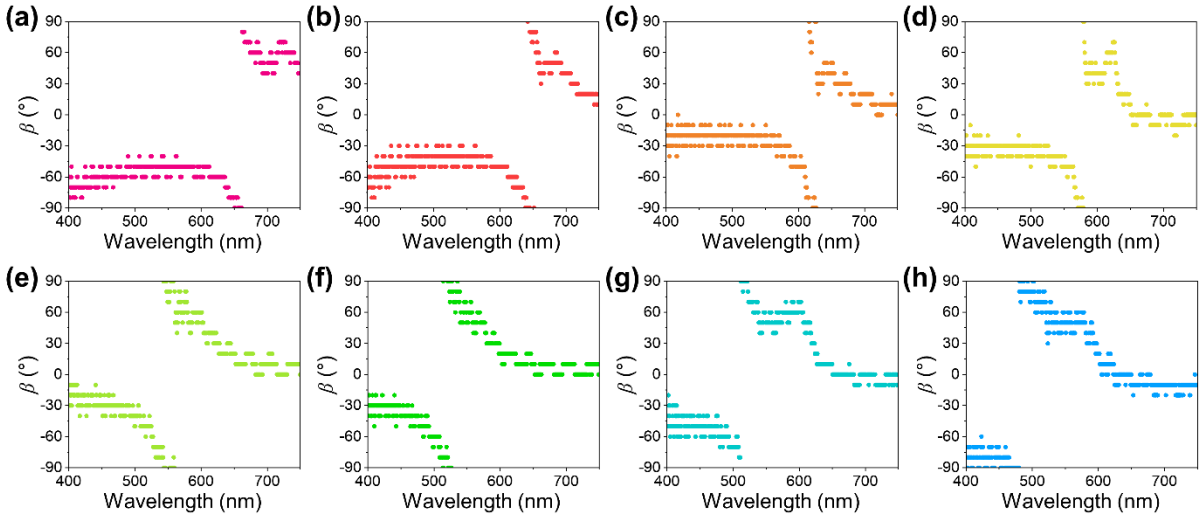

Figure S4. Sequential changes in the optical rotation of C-CLCE. a–h) Optical rotation of C-CLCE according to the applied compressive strain of ε_z values increasing from 0 to −0.28 at −0.04 intervals.

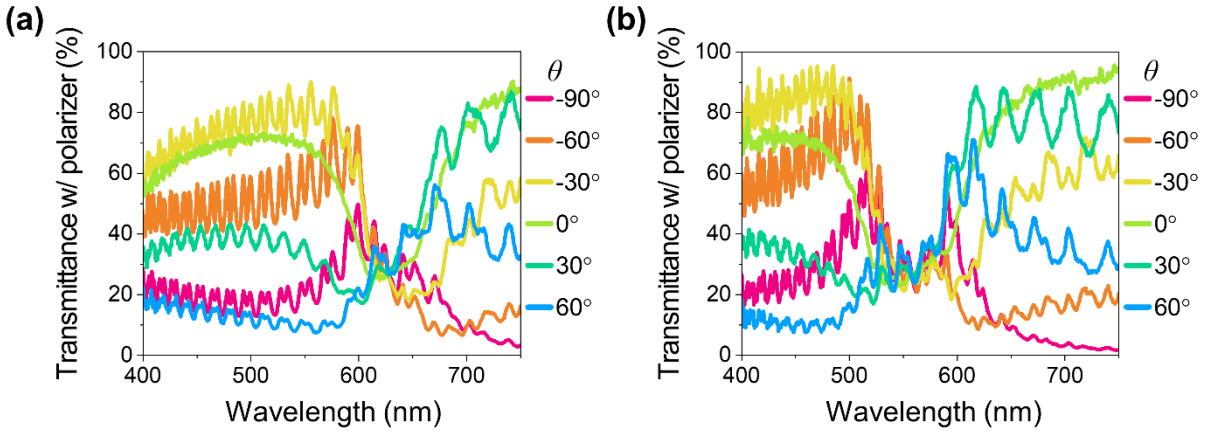

Figure S5. Transmittance of C-CLCE with top polarizer. a–b) Transmittance of C-CLCE measured while rotating the top polarizer from −90° to 60° at (a) $\varepsilon_z = -0.08$ and (b) $\varepsilon_z = -0.20$. The transmittance spectra were normalized by the transmittance of the two parallel polarizers with a 2mm-thick PDMS film.

Table S2. Summary of optical characteristics, including position of λ_c, $\Delta\lambda$, and the transmittance at λ_c for each S-CLCE.

ε_z	λ_c (nm)	$\Delta\lambda$ (nm)	Transmittance at λ_c (%)
0	689.2	69.4±0.9	50.2
−0.04	661.9	50.8±0.8	42.0
−0.08	626.6	47.0±0.4	35.3
−0.12	600.2	38.0±0.5	29.3
−0.16	567.1	35.7±0.3	21.6
−0.20	543.7	35.5±0.3	17.5
−0.24	510.0	38.4±0.3	27.1
−0.28	484.5	47.3±0.4	36.4

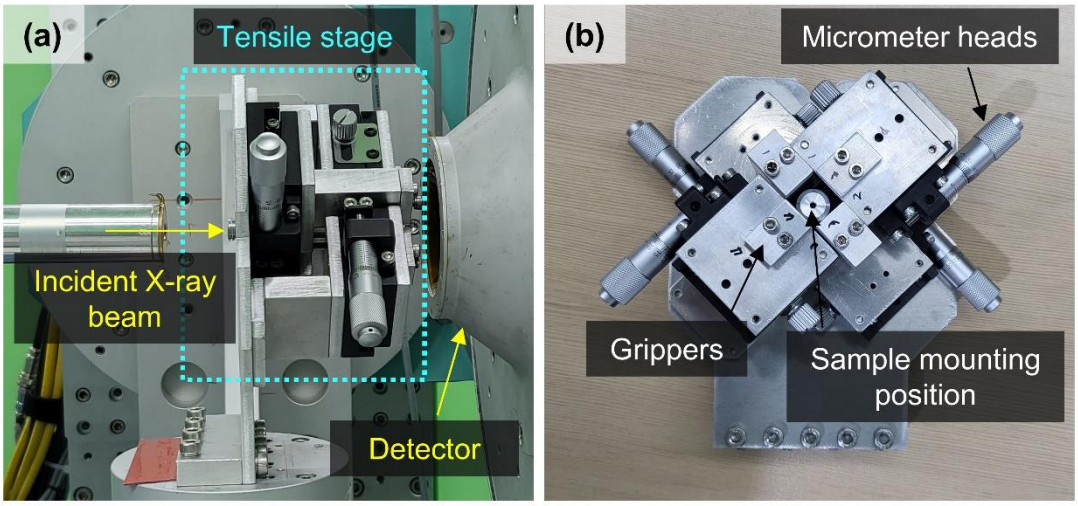

Figure S6. Equipment of wide-angle X-ray diffraction (WAXD) experiment. a–b) Photographs of (a) experimental setup for WAXD in transmission mode and (b) a customized tensile stage capable of both biaxial and uniaxial stretching.

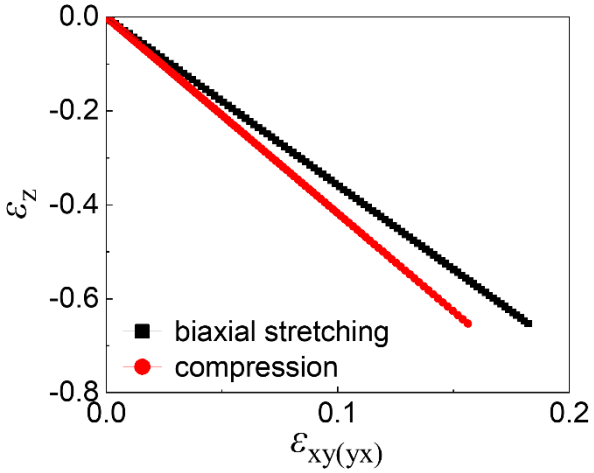

Figure S7. Theoretical longitudinal strain diagrams of CLCE film for biaxial stretching and compression.

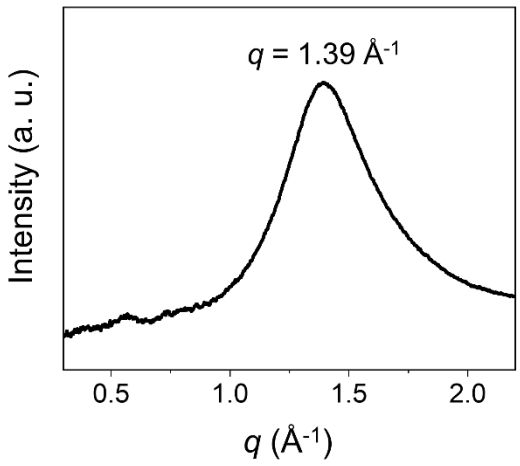

Figure S8. Line-cut profiles of 2D GIXD images of freestanding CLCE film without any strain.

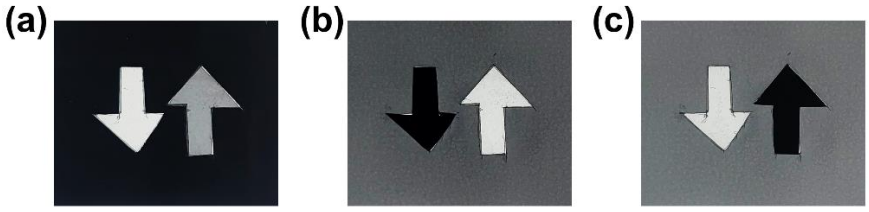

Figure S9. Patterned bottom polarizer without CLCE film. a–c) Photographs of patterned bottom polarizer without CLCE film taken while rotating the top polarizer at (a) $\theta' = -90°$ (b) $-50°$ and (c) 30°. The black color represents the cross-polarization state between the bottom and top polarizers.

Captions for Movies S1–S6

Movie S1. Reflection colors of C-CLCE. A multi-layered CLCE film shows a color shift from red to blue upon arbitrary mechanical compression. (2 times faster than real-time motion)

Movie S2. Reflection colors of S-CLCE. A multi-layered CLCE film shows a color shift from red to blue upon arbitrary mechanical stretching. (3 times faster than real-time motion)

Movie S3. Transmission colors of C-CLCE with two linear polarizers. A multi-layered CLCE film is placed between bottom and top linear polarizers. The top polarizer is fixed in front of the camera lens with θ set at 50° or −30°. A CLCE film exhibits various colors according to arbitrary mechanical compression and θ. (3 times faster than real-time motion)

Movie S4. Transmission colors of S-CLCE with two linear polarizers. A multi-layered CLCE film is placed between bottom and top linear polarizers. The top polarizer is fixed in front of the camera lens with θ set at 50° or −30°. A CLCE film exhibits various colors according to arbitrary mechanical stretching and θ. (3 times faster than real-time motion)

Movie S5. Color variation of C-CLCE with patterned bottom polarizers. A multi-layered CLCE film is placed between patterned bottom polarizer and top linear polarizer. The top polarizer is fixed in front of the camera lens with θ' set at −50°, 20° and 30°. The CLCE film is placed as close to the lens as possible to cover the entire shooting area with the uniform transmission colors of CLCE upon mechanical compression. Each video at a specific θ' is individually sped up to match the degree of arbitrary deformation between the videos.

Movie S6. Color variation of S-CLCE with patterned bottom polarizers. A multi-layered CLCE film is placed between patterned bottom polarizer and top linear polarizer. The top polarizer is fixed in front of the camera lens with θ' set at −50°, 20° and 30°. The CLCE film is placed as close to the lens as possible to cover the entire shooting area with the uniform transmission colors of CLCE upon mechanical stretching. Each video at a specific θ' is individually sped up to match the degree of arbitrary deformation between the videos.